



Contents lists available at ScienceDirect

Deep-Sea Research II

journal homepage: www.elsevier.com/locate/dsr2Tidal effect on the dense water discharge, Part 2: A numerical study[☆]Xiaorui Guan^{a,*}, Hsien-Wang Ou^a, Dake Chen^b^a Division of Ocean and Climate Physics, Lamont-Doherty Earth Observatory, Columbia University, 61 Route 9W, Palisades, NY 10964, USA^b The State Key Lab of Satellite Ocean Environment Dynamics, SIO, Hangzhou, China

ARTICLE INFO

Article history:

Accepted 27 October 2008

Available online 17 November 2008

Keywords:

Tidal shear dispersion
Dense water discharge
Gravity current
Numerical modelling

ABSTRACT

In Part 1 of this two-part paper, an analytical model is presented to examine the tidal effect on the dense water discharge. It is hypothesized that the tide-induced shear dispersion would augment the benthic-layer thickness to significantly enhance the spread of dense water on the shelf and its descent down the continental slope. Here in Part 2, we carry out a numerical process study to assess the analytical model and to aid the interpretation of the observed phenomenon in the western Ross Sea.

In this process study, we conduct numerical experiments for both passive and active tracer, and demonstrate the sharp contrast between the tidal and non-tidal cases whether on a flat or sloping bottom. In particular, on a slope as steep as the western Ross Sea, the model result from the non-tidal case shows that the dense water cannot descend much beyond the shelf break due solely to Ekman advection. When tides are included, however, the dense benthic layer would span several times the Ekman depth, which reduces the diabatic mixing across the density interface that would otherwise dilute the density anomaly, hence allowing the dense water to be more efficiently propelled by the Ekman flow and tidal diffusion. The model results are consistent with the analytical model, and also corroborated by the observations from AnSlope.

© 2009 Elsevier Ltd. All rights reserved.

1. Introduction

The High-Salinity Shelf Water (HSSW) is formed on the Antarctic shelves, and as it descends down the continental slope, it entrains the ambient less-dense Circumpolar Deep Water (CDW), and forms a benthic outflow into the adjacent deep ocean, providing the kernel for Antarctica Bottom Water (AABW) formation.

Since the western Ross Sea is important for the AABW formation, an NSF-funded project AnSlope was carried out there to address the physical processes on the Antarctic slope. CTD measurements were taken near Drygalski Trough, which showed that the dense water on the shelf descends all the way down to the lower slope in the benthic layer of 100–250 m thick. This thickness is several times the Ekman depth at that latitude, and hence cannot be due solely to the Ekman dynamics. The mean temperatures of the HSSW and the CDW are -1.6 and 1.2 °C, respectively, corresponding to a density difference of 0.4 kg m^{-3} .

Several mechanisms have been proposed for the descent of the HSSW. One prevailing idea is that the Ekman flow generated by the bottom friction would propel the dense water down the slope (Baines and Condie, 1998; Nagata et al., 1993; Condie, 1995; Shapiro and Hill, 1997). Other mechanisms also have been

proposed, including channeling by the submarine canyons (Chapman and Gawarkiewicz, 1995; Jiang and Garwood, 1995), and the transport by eddies (Jiang and Garwood, 1996; Gawarkiewicz and Chapman, 1995; Kikuchi et al., 1999), as both would break the rotational constraint on the down-slope motion.

The previous efforts to model the dense water discharge down the continental slope have sometimes adopted the streamtube approach (Smith, 1975), which considered only the bulk properties, but not the internal structure of the plume (Price and O'Neil Baringer, 1994). More sophisticated two- and three-dimensional numerical models also have been applied in the studies of dense water discharge. Jungclaus and Backhaus (1994) used a two-dimensional reduced-gravity model to study the topographic effect on the Denmark Strait Overflow. Ezer and Weatherly (1990) employed both a second-order turbulence closure scheme and an eddy-viscosity scheme in their two-dimensional z-coordinate primitive-equation model, and showed that the horizontal and vertical scales of the down-slope cold tongue are governed by the Ekman veering and Ekman depth, respectively. Moreover, complicated 3-D numerical models with different coordinate systems have been used to study the problem as well (Jiang and Garwood, 1995, 1996; Jungclaus and Mellor, 2000; Ezer and Mellor, 2000; Ezer, 2005, 2006). These models could resolve the instability features of the dense benthic layer such as eddies and sub-plumes, shedding further light on its dynamics.

Nevertheless, most of the previous numerical models (with the exception of Padman et al., 2009) have neglected the tides, an important feature in the AnSlope observations. The effectiveness

[☆] Lamont-Doherty Earth Observatory Contribution Number 7222.

* Corresponding author.

E-mail address: xguan@ldeo.columbia.edu (X. Guan).

of the tidal shear dispersion in passive tracer transport (Okubo, 1967), together with the prominent tidal current in the benthic layer as observed in the AnSlope (Gordon et al., 2004), motivated our process study. We carry out numerical experiments to elucidate the tidal rectified effect based on analytical study in Part 1 of this paper (Ou et al., 2009, referred henceforth as Part 1) and, specifically, to evaluate our hypothesis that the tides could augment the dense layer thickness and significantly enhance its descent down the slope.

Previous three-dimensional numerical studies have shown that eddy formation through baroclinic instability might be important for the dense water discharge, among others that would break the rotational constraint. The AnSlope observations have not indicated the prevalence of eddies in the benthic layer, since the descent angle of the dense water is relatively stable (Gordon et al., 2004). We do not exclude the possibly important role of eddy formation, but our purpose of this process study is to examine whether the tidal effect may significantly enhance the dense water descent on the slope. And since the proposed tidal effects are fully operative in the two-dimensional cross-shore plane, we employ in this paper, a two-dimensional configuration of a hydrostatic z -coordinate primitive-equation model. The tidal effect is demonstrated by the contrast between simulations with and without introducing tides into the model domain, which should be sufficient to evaluate our hypothesis in Part 1.

There have been many previous studies on the advantages and drawbacks of numerical models with different resolutions and vertical coordinates in simulating the dense water discharge. z -Coordinate models are not particularly favored against terrain and isopycnal-following models in the capability of simulating sufficient down-slope penetration of the dense plume, but if the vertical resolution is fine enough to resolve the benthic layer and the horizontal grid does not exceed its vertical grid divided by the maximum slope (Winton et al., 1998; Legg et al., 2006), z -coordinate models work well in propelling the down-slope transport. Ezer and Mellor (2004) also showed that with a 2.5 km horizontal resolution, the bottom boundary layer structure starts to converge to the observed overflows. z -Coordinate system is preferred in our simulations due to the steep bottom slope in AnSlope observations (0.06), and we adopt very fine vertical and horizontal resolutions that satisfy the above criteria to guarantee the effectiveness in simulating the dense water descent.

2. Model description

The numerical model we use to explore the dense water discharge is a primitive-equation, free-surface, coastal ocean model originally developed by Wang (1982, 1985). It has been applied to different coastal studies, such as the simulations of the upwelling front off the northern California coast (Chen and Wang, 1990), the tidal front in the Celtic Sea (Wang et al., 1990), and the internal tides in a coastal frontal zone (Chen et al., 2003), among others. In this model configuration, we use the Mellor and Yamada (1982) level 2.5 turbulence closure for vertical mixing, which has been well tested and discussed in many numerical studies of dense plume dynamics (Jiang and Garwood, 1995, 1996; Jungclauss and Mellor, 2000; Ezer and Mellor, 2000), and Smagorinsky's (1963) parameterization for horizontal mixing, which is essential for minimizing nonphysical mixing and maintaining a sharp front in the model (Chen et al., 2003). As we pointed out before, the model is configured on a two-dimensional cross-shore section, since our purpose is to isolate and elucidate the tidal effect, but not to simulate unstable eddies.

The resolution is quite high, with horizontal and vertical grid spacings of 600 and 10 m, respectively, in the sloping bottom

cases, which is adequate to resolve the Ekman layer about 30 m. Tides are imposed through the oscillation of the surface elevation at the offshore boundary of the model domain to produce a cross-shore tidal current amplitude of 20 cm s^{-1} , which corresponds to a tidal excursion distance around 5 km for diurnal tides. For all the experiments below (except for the semi-diurnal case) the model domain is placed at 65°N , representative of the high-latitude coastal oceans, where the semi-diurnal tides approach the inertial frequency, so the domain is placed at mid-latitude only for the semi-diurnal case hereinafter. At the inshore boundary, the temperature is fixed at -2°C with zero normal-gradient; the velocity satisfies the Orlanski open boundary condition. At the offshore boundary, Orlanski condition is imposed on temperature, while velocity has zero normal-gradient. The quadratic law friction is applied to the bottom boundary, with a drag coefficient of 0.0025.

Since the temperature effect dominates the density variation, we neglect for simplicity the salinity difference. The traditional "dam-break" technique is adopted: a vertical barrier that separates two water columns with different temperatures on the shelf is removed at time $t = 0$ to allow the density front to adjust. This technique has been widely used in numerical studies of coastal and continental shelf circulation in shallow seas (Wang, 1984; Oey and Mellor, 1993; Jiang and Garwood, 1995). The temperatures of the two water columns are -2 and 1°C , respectively, which results in a sigma- t difference of 0.3 kg m^{-3} , close to the observations, and a baroclinic deformation radius of about 8 km.

To evaluate the analytical model results in Part 1, we first treat temperature as a passive tracer to estimate how the benthic-layer properties change with varying forcing frequency in Section 3, in which both the bottom slope and density variation are excluded. We then include the density effect in Section 4 and bottom slope in Section 5 to address the additional physics which are important for the dense water discharge in the oceanic settings. In Sections 4 and 5, a surface heat loss of 100 W m^{-2} is imposed on a coastal strip of 20 km to simulate cooling in a coastal polynya.

3. Passive tracer on flat bottom

In Part 1, we extended the well-known physics of tidal shear dispersion to the genesis of the benthic layer of passive tracer, whose depth turns out to be several times the Ekman depth. We showed that apart from the singularity at the inertial frequency, both the benthic depth h_b (non-dimensionalized by Ekman depth) and the mean tidal diffusivity within the benthic layer k (non-dimensionalized by u'^2/f where u' is the tidal amplitude) generally increase with decreasing forcing frequency, as shown by the thick solid and dashed curves in Fig. 2.

Numerical experiments are carried out to validate the non-dimensionalization and to assess the results of h_b and k with varying forcing frequencies in the analytical model. As described in Section 2, we set an initial vertical front separating two homogeneous regions with different temperatures -2 and 1°C . Since temperature is treated as a passive tracer by removing the temperature dependence from the equation of state, the two water masses have no density difference. A weak background stratification is nonetheless imposed to curtail the unphysical vertical mixing, and we set the upper bound of vertical diffusivity coefficient ν_{max} to be $500 \text{ cm}^2 \text{ s}^{-1}$, and the background ν to be $10 \text{ cm}^2 \text{ s}^{-1}$ unless otherwise stated.

The front would remain intact until we introduce the oscillatory forcing, which broadens the front near the bottom except for the inertial frequency, indicating a locally significant tidal diffusivity as predicted by Part 1. The benthic-layer depth h_b

is several times the Ekman depth, which agrees with the deduction of Part 1 that the tidal diffusivity remains significant on vertical scales much greater than the Ekman depth. Here the top of benthic layer is defined by the e-folding scale of the property field, and the mean tidal diffusivity k in the benthic layer is estimated as the mean expansion rate of the front on the bottom, i.e., $l_t^2/2t$ where l_t is the cross-section distance where the concentration is one standard deviation away from the mean. The temporal revolution of the front expansion reveals that l_t^2 grows nearly linearly with time t , so it is reasonable to pick any time span to calculate k .

First, we would like to evaluate the non-dimensionalization of the variables in the analytical model of Part 1, specifically, benthic depth scaled by the Ekman depth and tidal diffusivity by $[u']^2 f^{-1}$. Two sets of sensitivity experiments are conducted to qualitatively examine them. In the first set, we fix the tidal amplitude u' at 20 cm s^{-1} and change the maximum vertical diffusivity v_{max} on the bottom from 250 to $1000 \text{ cm}^2 \text{ s}^{-1}$; in the second set, we then fix v_{max} at $500 \text{ cm}^2 \text{ s}^{-1}$, and the tidal amplitude varies from 10 to 50 cm s^{-1} . The results of the two experiment sets are plotted in Fig. 1(A) and (B), respectively. It is seen that the tidal diffusivity k remains unchanged with varying vertical diffusivity and grows approximately quadratically with increasing tidal amplitude, which supports that tidal diffusivity should be scaled by square of the tidal amplitude, and is independent of the vertical diffusivity. The benthic depth, however, varies approximately as a square root of the vertical diffusivity, which supports its scaling by the Ekman depth. The benthic depth is also thicker if we increase the tidal amplitude, which is reasonable since stronger tides introduce stronger tidal diffusivity to overcome the background stratification, a factor not included in the analytical model, as we shall explain further later.

As the non-dimensionalization is confirmed, we would like to examine the dependence of non-dimensionalized h_b and k on varying forcing frequencies. Five experiments are implemented with different forcing frequencies: (a) low frequency with a period of four days; (b) sub-diurnal with a period of two days; (c) diurnal; (d) inertial and (e) semi-diurnal. The model results of h_b and k are marked by hollow circles and squares, respectively, in Fig. 2, with the corresponding property fields and velocity profiles shown in Fig. 3(A) and (B). As evident in Fig. 2, the dependency of non-dimensionalized h_b and k on the forcing frequency in the

numerical experiments compares favorably with the analytical solutions. Specifically, the non-dimensionalized benthic-layer depth h_b decreases from 8 to 3 (except for the singularity at the inertial frequency) and k from the order of 0.1 to 0.001 as the tidal frequency increases from low frequency to semi-diurnal. When the inertial frequency is approached, however, the current shear vanishes and the benthic layer extends through the whole water depth.

The analytical model assumes a constant vertical diffusivity, so the benthic depth is governed solely by the shape of the tidal diffusivity profile, but not its absolute value. In our numerical experiments, however, the vertical diffusivity is Richardson-number dependent, and there is an additional physical factor associated with the background density stratification included to avoid the unrealistic mixing. Because of this, stronger tidal amplitude would result in a larger absolute value of tidal diffusivity and thus a thicker benthic layer, even though its profile remains the same shape. Nonetheless, the experiments support the essential frequency dependence of the benthic depth predicted by the analytical model.

4. Dense water on a flat bottom

With the tidal diffusivity favorably compared with the analytical model, we shall next study the dispersion of the dense water, with temperature no longer treated as a passive tracer and its effect on the density field included. In fact, several physical processes may contribute to the horizontal spreading of the dense benthic water in our model: the geostrophic adjustment, the Ekman advection and the tidal dispersion. In order to isolate their individual effect, we incrementally include these processes into our numerical experiments.

Fig. 4 shows the temporal evolution of the temperature right above the bottom when tides are imposed. The temperature field varies rapidly during the initial adjustment to geostrophy (within the first day), and then the Ekman advection dominates, until it notably slows down after 3 days and the tidal diffusivity becomes important. After 20 days, the time-varying term is one-order magnitude smaller than the mean advective term in the tidal cases. So in the following experiments of this section, it is sensible to take the temperature field after 3 days as the quasi-steady state

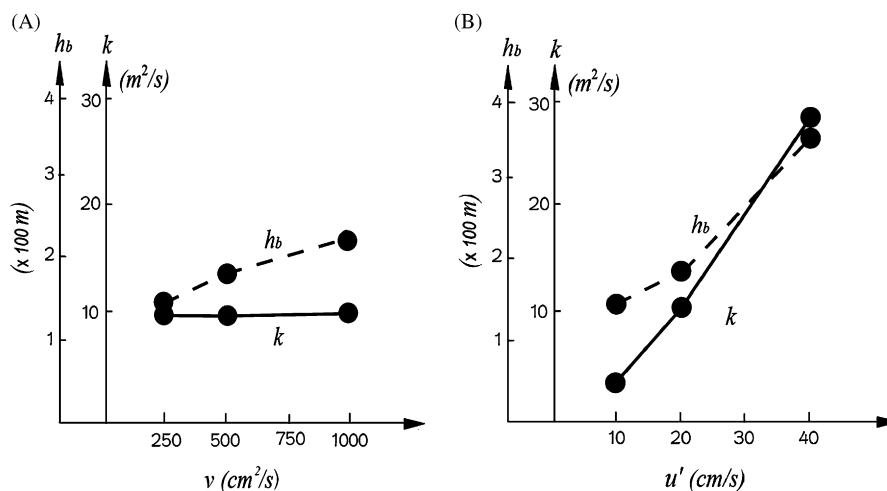


Fig. 1. The dimensional benthic depth h_b and tidal diffusivity k plotted against the vertical diffusivity v (A) and tidal amplitude u' (B). The solid and dashed lines connect the experimental points (circles). The tidal diffusivity k remains relatively unvarying with different vertical diffusivity, and grows approximately quadratically with increasing tidal amplitude. The benthic depth h_b varies approximately as a square root of the vertical diffusivity, which validates its scaling by Ekman depth. The benthic depth is also thicker with increasing tidal amplitude.

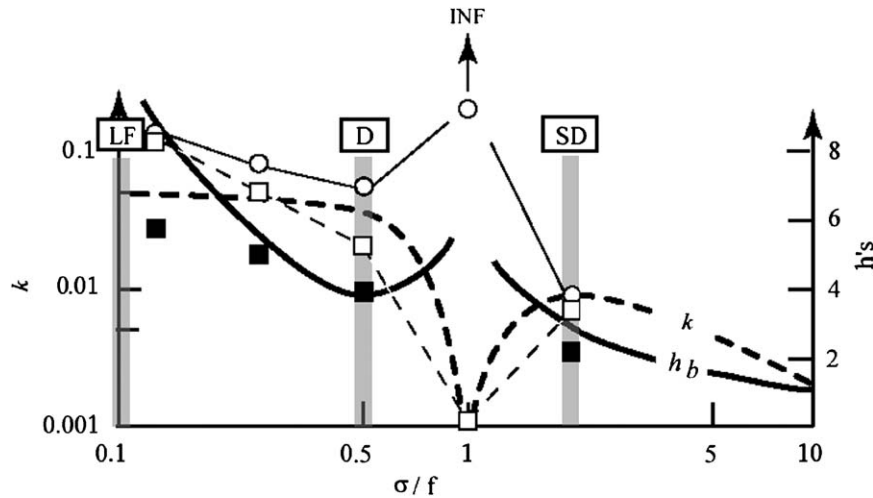


Fig. 2. The thick lines are the variables calculated from the analytical model. The thick solid curve is the analytical benthic-layer depth (h_b , non-dimensionalized by the Ekman depth), and the thick dashed curve is the mean tidal diffusivity k (scaled by u'^2/f , with u' being the tidal amplitude). The thin lines connect the corresponding values from numerical experiments, h_b marked by hollow squares and k by circles. The h_b in active tracer cases are marked by filled squares. Shaded columns denote semi-diurnal (SD) tides in the mid-latitude, diurnal (D) and low-frequency (LF) forcing in high-latitude.

for the non-tidal case dominated by Ekman advection, and 20 days for the tidal case. Since the model does not contain frontogenesis process to maintain the density field against slow diffusion, we expect it eventually homogenize over long-time integration.

4.1. Geostrophic adjustment

We first consider the spreading due solely to geostrophic adjustment. The Ekman friction is removed by setting bottom drag coefficient to be zero. The initial imbalance causes the front to tilt until the geostrophic balance is achieved. The adjustment is scaled by the inertial period, hence achieved within the first one day when the temperature field is as shown in Fig. 5A. We define the front edge by the e-folding scale of the source temperature, i.e. the 0 °C isotherm. The numerical result shows that the inclination of the front pushes the dense water to spread horizontally by 10 km approximately, about one deformation radius, as expected from the geostrophic dynamics.

4.2. Ekman advection

We now include the bottom friction, so that an Ekman flow is generated in the benthic layer accompanying the geostrophic along-shore current, which would propel the dense water offshore. The dense water is confined within the thin Ekman layer, which is about 30 m. The front advancing notably slows down after about 3 days when the system achieves a quasi-steady state. The model result shows that the Ekman friction causes the benthic dense water to advance another deformation radius R_c beyond the geostrophic front (Fig. 5B), with a total spreading distance of about 17 km, which agrees with the analytical prediction ([4.7] in Part 1).

To examine how the vertical diffusivity would affect the benthic-layer depth and horizontal spreading by the Ekman dynamics, we increase ν_{max} from 500 to 1000 $cm^2 s^{-1}$. As expected, the benthic depth increases by about a half, because of its square root dependence on vertical diffusivity, while the horizontal spreading distance remains unchanged, which further supports the analytical result that the deformation radius is the relevant scale for the spreading by the Ekman dynamics.

4.3. Tidal dispersion

To show how the tidal dispersion enhances the horizontal spreading, tides are imposed with tidal amplitude of 20 $cm s^{-1}$. After 20 days when a quasi-steady state is achieved, it is seen that the dense benthic layer in the diurnal case has further spread another horizontal distance of more than 8 km (Fig. 6A) compared with the above non-tidal experiment, which is about another deformation radius and beyond the tidal excursion distance (5 km). Similar to the passive tracer case in Section 3, the dense benthic layer has a thickness several times the Ekman depth due to the tidal dispersion, and the front on the bottom is much broadened (Figs. 6 and 7).

The benthic-layer depth is about 100 m for the diurnal case, and 80 m for the semi-diurnal case (Figs. 6 and 7). It is seen that the tidal rectified effect significantly enhances the horizontal spreading of the active tracer in the benthic layer, and the front is considerably diffused horizontally as in the passive tracer cases, again indicating significant tidal diffusion within the benthic layer. Moreover, the thickness of the benthic depth is several times the Ekman depth, with density stratification well above the bottom shear regime. So the interfacial diabatic mixing of the dense water with its ambience is suppressed (Figs. 6B and 7B) compared to the non-tidal case where the stratification is aligned with shear depth, due to its Richardson-number dependence. Since the interfacial diabatic mixing is the main mechanism to counter the Ekman advection in the non-tidal experiment, its suppression in tidal cases would augment the horizontal spreading of the dense water, and hence the tidally averaged Ekman flow due to altered stratification. As shown in Fig. 8, both the along-shore and the offshore velocities in the benthic layer are increased by a half after 2 days of model run, suggesting an enhanced horizontal spreading of dense water. Hence the two mechanisms: considerable tidal diffusivity and amplified Ekman flow would both contribute to the horizontal spreading (Fig. 9).

In order to know the relative importance of the two mechanisms: tidal diffusivity and Ekman advection, we need to compare the two terms: $k(\partial^2 C/\partial x^2)$ and $u_E(\partial C/\partial x)$, where u_E is the tidal-mean offshore velocity in the benthic layer, and C is the density or property field. Given the mean offshore velocity u_E to be 1 $cm s^{-1}$ after 20 days of model run, and k to be 12 $m^2 s^{-1}$ estimated from the passive tracer cases with diurnal tides, and the horizontal

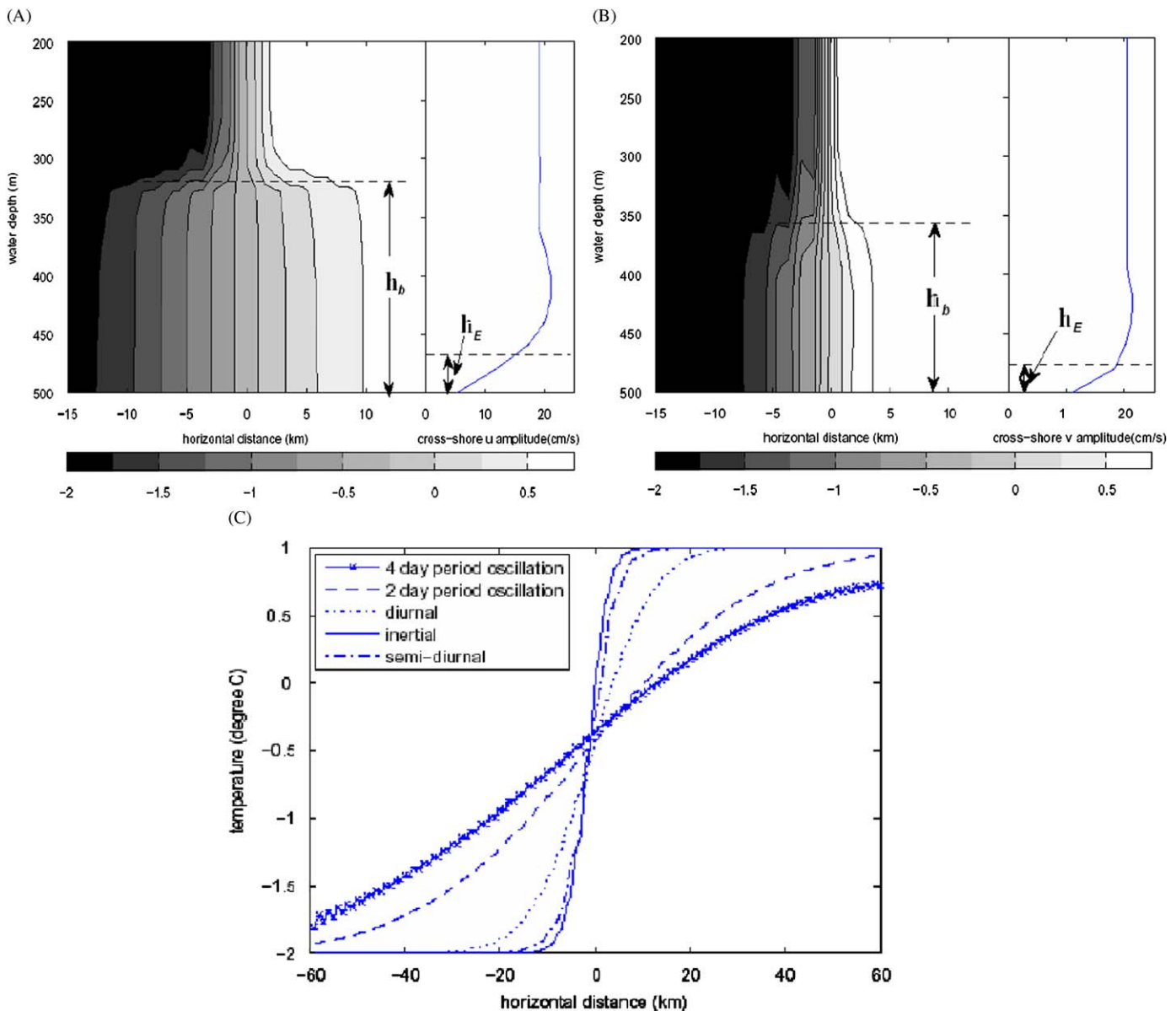


Fig. 3. The model solutions of numerical experiments for the passive tracer (temperature as a proxy) with different frequencies, after 50 days of model run. (A) Left panel: the mean temperature field for the diurnal tide, with the sharp front initially placed at the origin; contour interval is $0.25\text{ }^{\circ}\text{C}$; right panel: the cross-shore velocity amplitude. h_b and h_E have depths of about 180 and 30 m, respectively. (B) Same as (A) except for the semi-diurnal tide, and h_b and h_E are about 140 and 20 m, respectively. (C) The horizontal temperature distribution at 40 m above the bottom for five different frequencies.

scale of the property variation to be 20 km, the Ekman advection term is one order of magnitude larger than the tidal diffusion term. However, it needs to be stressed that although the contribution of the Ekman advection seems larger than that of tidal diffusion, it is the tidal diffusivity that augments the benthic-layer thickness, hence preconditions the amplification of the mean Ekman advection.

To evaluate further the validity of the functional dependence of the benthic layer depth h_b on varying tidal frequencies in active tracer cases, we conduct the numerical experiments with the same five different oscillatory frequencies in Section 3, except now, the temperature dependence is activated in the equation of state. The results of h_b are marked in Fig. 2 by filled squares. Except for the singularity of inertial frequency, h_b decreases with increasing frequency as well, the same pattern as in the passive tracer case. The benthic depth h_b is about one-third thinner than those in the passive tracer experiments (marked by hollow squares), because the benthic layers are now topped by strong

density stratification and cannot freely span vertically as the passive tracer case. Nevertheless, the benthic layer is still several times thicker than the Ekman depth, nor does it change the decreasing trend of h_b with increasing frequencies. At the inertial frequency, there is no tidal dispersion for the lack of shear, so the benthic depth is undefined in this case.

5. Dense layer on a slope

As a final step in our incremental physics, we include a linear bottom slope to examine the descent of the dense water. The slope introduces additional physics into the dense water discharge process. Without tides, the geostrophic along-shore flow on the slope is mainly regulated by the interfacial slope steepness according to Nof (1983), and so is the offshore Ekman flow. When tides are imposed, the tidal rectification effect in the flat bottom cases would still be effective qualitatively, except that given the

same tidal amplitude on the shelf, the local tidal amplitude on the slope is decreased as the water depth increases.

In order to study how the steepness of the bottom slope affects the dense water discharge, three experiments with different steepness s (0.002, 0.006 and 0.02) are conducted. The slope width is fixed, so different steepness corresponds to different depth of the abyssal ocean. Since our purpose is to study the dense water descent on the slope, we set the slope width to be broad enough for the dense water to remain on the slope when the quasi-steady state is attained after 30 days. The tidally-averaged offshore velocity close to the shelf break u_E doubles from 2 to 4 cm s^{-1} as s increases from 0.002 to 0.02. At the same time, the

horizontal spreading of the front L increases from 31 to 38 km, while the vertical drop beyond the shelf break H from 50 to 700 m. The growth of horizontal spreading L is milder than that of the mean Ekman flow at the shelf break u_E . That is because, both the Ekman flow and tidal diffusivity contribute to the horizontal spreading, and for a fixed tidal amplitude on the shelf, the local tidal amplitude gets smaller as the dense water proceeds down the slope, resulting in a weaker tidal diffusivity thus less horizontal advance. While the growth of vertical drop of the front H is faster than that of u_E due to the fact that vertical drop increases with the steepness for the same horizontal spread.

The gradient of western Ross Sea near Drygalski Trough is around 0.06. The water depth increases from 500 m on the shelf to 2000 m in the deep ocean within a narrow slope width of 25 km. Again we carry out the tidal (diurnal) and non-tidal experiments to better demonstrate the tidal effects. In the non-tidal case, the dense water remains confined to the thin shear depth, hence gets diffused rapidly by the vertical mixing with a horizontal distance of only less than 10 km, consistent with Part 1, and it does not ascend much beyond the shelf break, because the mixing with the ambient water would dilute the initial density anomaly (Fig. 10A). It suggests that Ekman dynamics alone is not sufficient to propel the dense water into the deep ocean. This is in sharp contrast with the tidal case where the dense water propagation is much more efficient. The front descends all the way down to the abyssal plain because of the narrow slope width, and by the end of 30 days, the slope is blanketed by the cold water with temperature between -1.5 and -0.5 $^{\circ}\text{C}$, much colder than that in the non-tidal case (Fig. 10B).

In addition to propelling the offshore discharge of the dense water, tides also alter the vertical structure of the benthic layer on the slope. Figs. 10C–F are the vertical profiles of both tidal and non-tidal experiments. The cross-shore temperature distribution and vertical profiles of offshore and along-shore velocities plotted in Figs. 8B–D are the tidal-mean values, while the profiles of vertical diffusivity and temperature in Figs. 10E and F are at the slack between flood and ebb. Because the front is diffused considerably, the top of the benthic layer for the non-tidal case

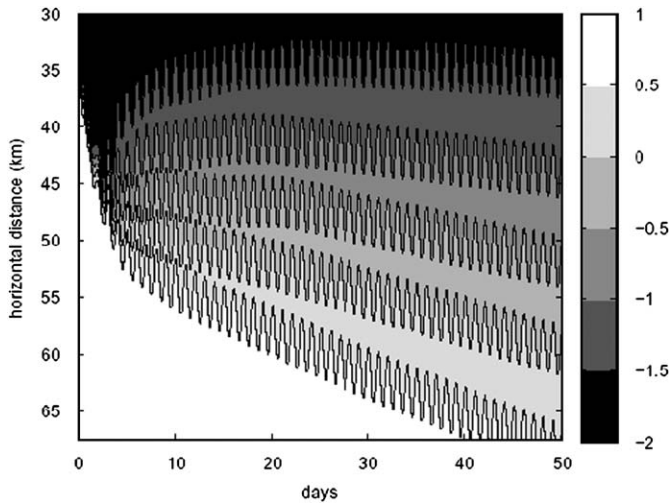


Fig. 4. The temporal evolution of the temperature on the bottom with the diurnal tides in the active tracer experiments. The front is initially placed at the horizontal distance of 30 km. The temperature field varies rapidly due to Ekman advection and it notably slows down after the first 3 days. And then the tidal diffusivity becomes important, until after 20 days the time-varying term is one-order magnitude smaller than the advective term in the tidal cases, and the quasi-steady state is attained.

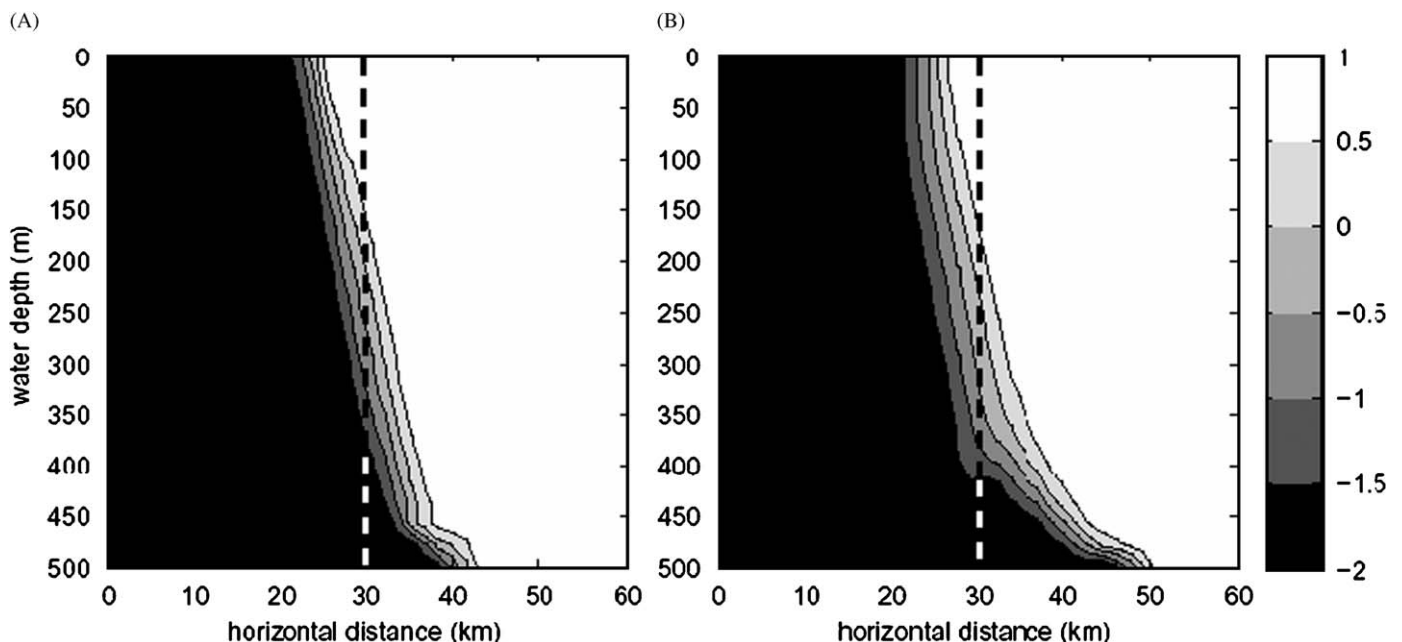


Fig. 5. The temperature fields when the quasi-steady states are reached. (A) The bottom is free-slip so there is no Ekman flow, and the geostrophic adjustment slows down within 1 day. (B) The bottom stress is turned on so that both geostrophic adjustment and Ekman dynamics are in effect, and the quasi-steady state is reached after 3 days. The contour interval is 0.5 $^{\circ}\text{C}$. The dash lines are the locations of the initial front.

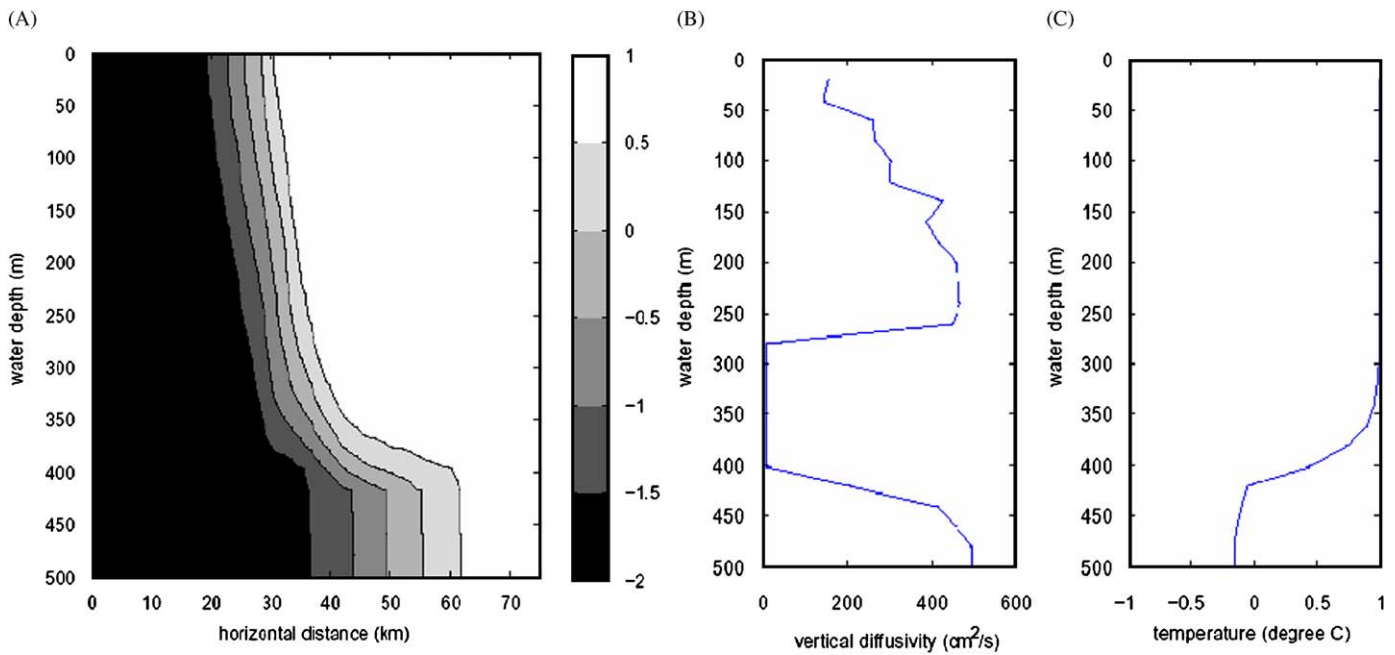


Fig. 6. (A) Same as Fig. 5 but at 20 days, with a diurnal forcing of 20 cm s^{-1} in tidal amplitude; (B) the profile of vertical diffusivity at an offshore distance of 50 km and (C) same as (B) but for temperature. It is seen that the benthic-layer depth is about 100 m for the diurnal case, several times the Ekman depth due to the tidal dispersion, and the front on the bottom is much broadened.

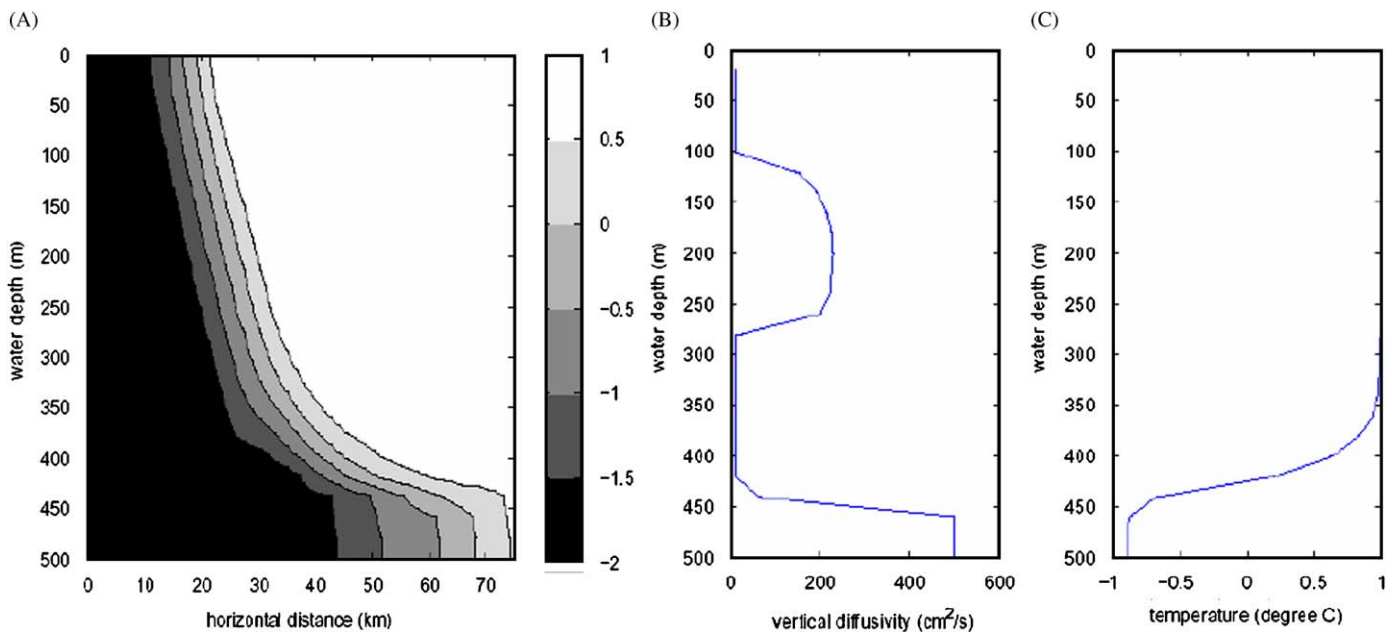


Fig. 7. Same as Fig. 6, but forced with a semi-diurnal tide (in the mid-latitude). The benthic-layer depth is about 70 m for the diurnal case, several times the Ekman depth.

cannot be defined by the e-folding scale of the property distribution as in previous sections. Actually, it is more sensible to define the benthic layer by the vertically uniform temperature field on the bottom. The benthic-layer thickness in the tidal case is several times that of the non-tidal case, both on the shelf and slope. According to the profiles in Fig. 10F, which show the temperatures at the offshore location close to the shelf break where the water depth is 800 m, the benthic depth in the tidal case is 150 m, 6 times that of non-tidal case (25 m), which is consistent with the analytical results shown in Fig. 2. The vertical

diffusivity (Fig. 10E) at the interface is $500 \text{ cm}^2 \text{ s}^{-1}$ for the non-tidal case, suggesting strong diabatic mixing with the ambient water at the interface. For the tidal case, it decreases to $200 \text{ cm}^2 \text{ s}^{-1}$ since the interface is above the shear layer, which supports our hypothesis that the reduced vertical diffusivity across the top of the benthic layer would augment the dense water descent when tides are imposed. The vertical gradient of along-shore velocity follows the thermal wind relation given the corresponding density distribution, as assumed in the analytical model of Part 1. The offshore velocity is less than one-half of the along-shore velocity

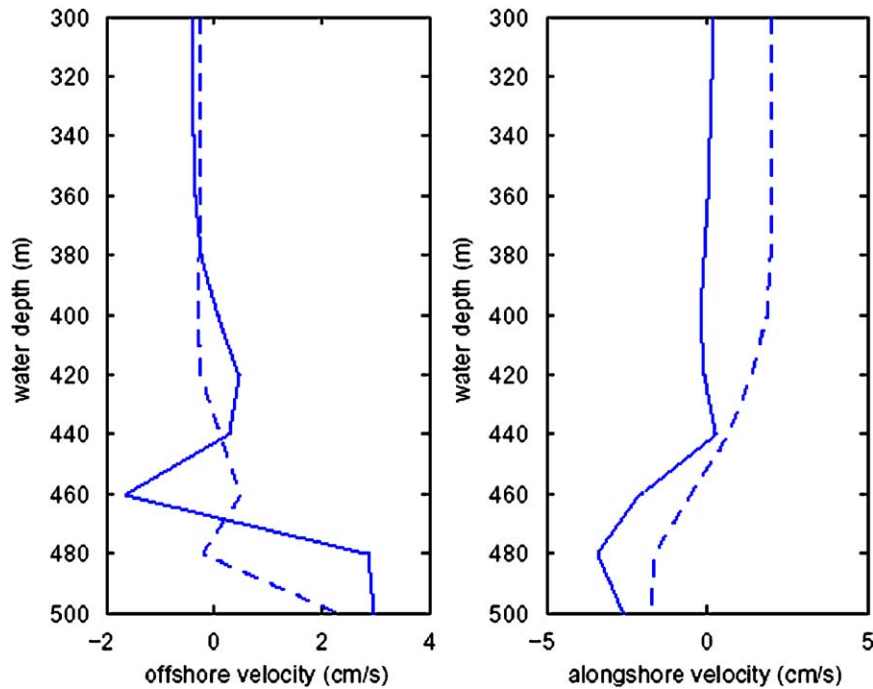


Fig. 8. The offshore and the along-shore velocities in non-tidal (dash) and tidal cases (solid) for active-tracer experiments on a flat bottom at $t = 2$ days. In the benthic layer, both are increased by about a half in the tidal vs. non-tidal cases, suggesting an enhanced horizontal spreading by tides.

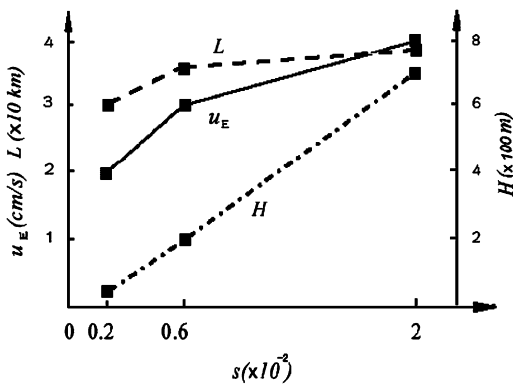


Fig. 9. The mean offshore velocity near the shelf break (u_E , solid), the horizontal spreading (L , dashed) and the vertical drop (H , dash-dotted) of the dense water beyond the shelf break plotted against the increasing steepness of the bottom slope s .

as shown in Part 1, because the numerical model employs quadratic bottom friction instead of the non-slip condition. Both the mean along-shore and cross-shore velocities in the benthic layer are much stronger in tidal case than that in the non-tidal case. The Ekman dynamics alone can only produce a cross-shore flow of less than 3 cm s^{-1} corresponding to an along-shore flow of 10 cm s^{-1} . The tides can amplify the cross-shore and along-shore flow to the amplitude of 6 and 40 cm s^{-1} , respectively. Specifically, the offshore velocity is 2 times stronger, which contributes to a much greater cross-shore advance of the dense water. Enhanced dense water descent would produce a sharper density contrast with the ambient water compared to the non-tidal case, which further increases the along-shore velocity in the benthic layer according to thermal wind relation. This in turn would induce a stronger offshore Ekman flow, a positive feedback that amplifies the tidal effect.

6. Discussion and summary

A numerical process study from a primitive-equation model agrees with predictions in Part 1, and supports our hypothesis that the tidal dispersion may significantly enhance the dense water spread and descent down the slope.

In our numerical experiments of tidal dispersion of the passive tracer, the benthic depth h_b spans several times the Ekman depth; and the mean tidal diffusivity k attains large amplitude which is sufficient to produce prominent dispersion; and both h_b and k increase with decreasing forcing frequency from 4-day period to semi-diurnal (except for the singularity at the inertial frequency), which is consistent with the analytical results in Part 1. As to the dense water spreading on a flat bottom, the geostrophic adjustment takes place rapidly within 1 day, resulting in a horizontal spreading about one deformation radius; while the Ekman advection remains prominent and is able to advance the front another one deformation radius or so before a quasi-steady state is achieved after 3 days; however, the tidal dispersion would broaden and propel the front even further, due to considerable tidal diffusivity and enhanced offshore Ekman flow, preconditioned by the thick benthic layer and the reduced vertical diffusivity on its top. When we include a bottom slope to examine the descent of dense water on a broad slope width, its offshore flow, horizontal spreading and vertical reach all increase with steeper slope.

In the simulations of the AnSlope case, the Ekman dynamics alone is not sufficient to explain its down-slope descent, nor the observed benthic-layer thickness. The tidal case, however, demonstrates the prominent capability of tides in propelling the offshore discharge by altering the vertical profiles of density and velocity. The top of the benthic layer spans far above the shear layer, so the diabatic mixing across the interface is much reduced compared with the non-tidal case, which deters the dilution of the dense water and propels its cross-shore spread. It agrees with the analytical results in Part 1 and is also consistent with the observations as well.

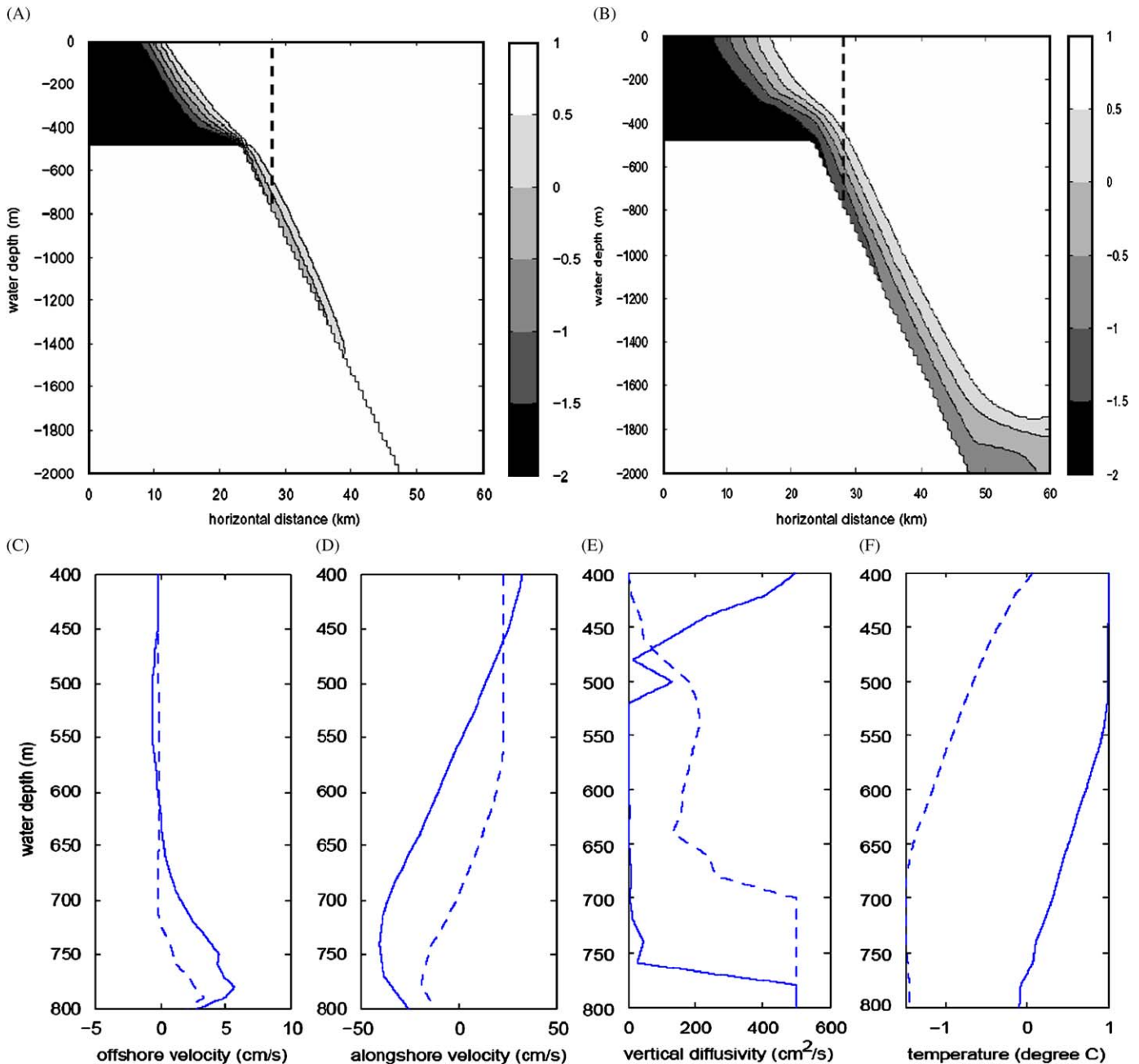


Fig. 10. Upper panels: temperature fields after 30 days for (A) non-tidal, (B) diurnal-tidal cases (tidal mean). The front is initially set at 18 km and contour interval is 0.5 °C. Lower panels: tidal (solid) vs. non-tidal (dashed) profiles of (C) offshore velocity, (D) along-shore velocity, (E) vertical diffusivity, and (F) temperature at the offshore location where the water depth is 800 m (as indicated by vertical dashed lines in (A) and (B)). Profiles (C) and (D) are tidal means, and (E) and (F) are at the slack between flood and ebb.

Baines and Condie (1998) attributed the thick benthic layer whose top is well beyond that of the Ekman layer to the high level of production rate of the dense water, while leaving the theory of how the benthic-layer thickness grows over the Ekman layer incomplete. Our two-dimensional numerical process study provides a possibility that tidal effect could account for its vertical span without considering the eddy turbulence above the Ekman layer. Shapiro and Hill (1997) produced a benthic layer that is twice the depth of the Ekman layer using entrainment parameterizations with a two-dimensional reduced-gravity model, while we could obtain a much thicker benthic-layer depth that seems to agree with observations better. Diabatic mixing is

present in our primitive-equation model, while it is not in the reduced-gravity models. Padman et al. (2009) also have produced the enhanced depth-integrated down-slope transport of dense water in northwest Ross Sea by the increased benthic mixed-layer depth with their high-resolution baroclinic tide model, a confirmation of our process study.

Though our simulations are for the purpose of process studies, we could still make some comparison of the numerical results with the mooring measurements in AnSlope, as some of the model configurations in Section 5 are set according to the observations. Our model results compare well with the observations in phase difference between the temperature and the cross-shore velocity.

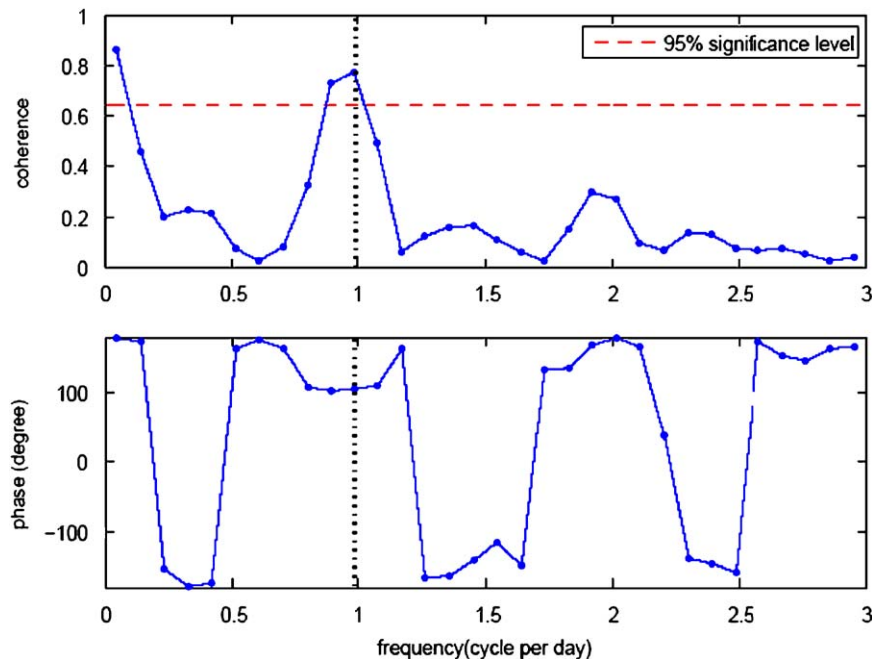


Fig. 11. Coherence and phase of observed temperature and cross-shore velocity at a lower slope site from AnSlope 1 (20 m above the bottom at the depth of 1770 m). Sampling interval is half an hour and the values have been averaged over eight frequency bands. Diurnal frequency is marked by the vertical dotted line, which has a phase angle of 105° . The angle is consistent with that from the numerical model (100°). (The data are the courtesy of Alejandro H. Orsi.)

Given the time series of temperature and cross-shore velocity measured 20 m above the bottom, on the lower slope where the water depth is 1772 m, we did the coherence and phase difference calculation (as shown in Fig. 11). The observed temperature and cross-shore velocity show high coherence at diurnal tidal frequency, and the phase difference at 1 cpd is about 105° , that is close to the 100° which we obtained from the model, both of which would clearly introduce a considerable down-slope tidal heat flux.

Acknowledgements

This study has benefited from discussions with AnSlope (a project funded by NSF/OPP) participants, as well as comments from anonymous reviewers. This work was funded by the National Science Foundation through grants OPP-0125177 and ANT-0538148.

References

- Baines, P.G., Condie, S., 1998. Observations and modeling of Antarctic downslope flows: a review. In: Jacobs, S., Weiss, R. (Eds.), *Ocean, Ice and Atmosphere: Interactions at the Antarctic Continental Margin*, Antarctic Research Series, vol. 75. AGU, Washington, DC, pp. 29–49.
- Chapman, D.C., Gawarkiewicz, G., 1995. Offshore transport of dense HSSW in the presence of a submarine canyon. *J. Mar. Res.* 53, 897–928.
- Chen, D., Wang, D.-P., 1990. Simulating the time-variable coastal upwelling during CODE 2. *J. Mar. Res.* 48, 335–358.
- Chen, D., Ou, H.-W., Dong, C., 2003. A model study of internal tides in coastal frontal zone. *J. Phys. Oceanogr.* 33, 170–187.
- Condie, S.A., 1995. Descent of dense water masses along continental slopes. *J. Mar. Res.* 53, 897–928.
- Ezer, T., 2005. Entrainment, diapycnal mixing and transport in three-dimensional bottom gravity current simulations using the Mellor–Yamada turbulence scheme. *Ocean Model.* 9 (2), 151–168.
- Ezer, T., Mellor, G.L., 2004. A generalized coordinate ocean model and a comparison of a bottom boundary layer dynamics in terrain following and in z -level grids. *Ocean Model.* 6, 379–403.
- Ezer, T., Weatherly, G.L., 1990. A numerical study of the interaction between a deep cold jet and the bottom boundary layer of the ocean. *J. Phys. Oceanogr.* 20, 801–816.
- Gawarkiewicz, G., Chapman, D.C., 1995. A numerical study of dense water formation and transport on a shallow, sloping continental shelf. *J. Geophys. Res.* 100, 4489–4507.
- Gordon, A.L., Zambianchi, E., Orsi, A., Visbeck, M., Giulivi, C.F., Whitworth, T., Spezie, G., 2004. Energetic plumes over the western Ross Sea continental slope. *Geophys. Res. Lett.* 31, L21302.
- Jiang, L., Garwood Jr., R.W., 1995. A numerical study of three-dimensional dense bottom plumes on a Southern Ocean continental slope. *J. Geophys. Res.* 100, 18471–18488.
- Jiang, L., Garwood Jr., R.W., 1996. Three-dimensional simulations of overflows on continental slopes. *J. Phys. Oceanogr.* 26, 1214–1233.
- Jungclauss, J.H., Backhaus, J.O., 1994. Application of a transient reduced gravity plume model to the Denmark Strait overflow. *J. Geophys. Res.* 99 (C6), 12375–12396.
- Jungclauss, J.H., Mellor, G.L., 2000. A three-dimensional model study of the Mediterranean outflow. *J. Mar. Syst.* 24, 41–66.
- Kikuchi, T., Wakatsuchi, M., Ikeda, M., 1999. A numerical investigation of the transport process of dense HSSW from a continental shelf to a slope. *J. Geophys. Res.* 104, 1197–1210.
- Legg, S., Hallberg, R.W., Girton, J.B., 2006. Comparison of entrainment in overflows simulated by z -coordinate, isopycnal and non-hydrostatic models. *Ocean Model.* 11 (1–2), 69–97.
- Mellor, G.L., Yamada, T., 1982. Development of a turbulence closure model for geophysical fluid problems. *Rev. Geophys. Space Phys.* 20, 851–875.
- Nagata, Y., Kimura, R., Honji, H., Yamazaki, Y., Kawaguchi, K., Hosoyamada, T., 1993. Laboratory experiments of dense water descending on continental slope. In: Teramoto, T. (Ed.), *Deep Ocean Circulation, Physical and Chemical Aspects*. Elsevier, Amsterdam, pp. 333–350.
- Nof, D., 1983. The translation of isolated cold eddies on a sloping bottom. *Deep Sea Res.* 30, 171–182.
- Oey, L.-Y., Mellor, G.L., 1993. Subtidal variability of estuarine outflow, plume, and coastal current: a model study. *J. Phys. Oceanogr.* 23, 164–171.
- Okubu, A., 1967. The effect of shear in an oscillatory current on horizontal diffusion from an instantaneous source. *Int. J. Oceanol. Limnol.* 1, 194–204.
- Ou, H.-W., Guan, X., Chen, D., 2009. Tidal effect on the dense water discharge: Part 1—Analytical model. *Deep-Sea Research II*, this issue [doi:10.1016/j.dsr2.2008.10.031].
- Padman, L., Howard, S.L., Orsi, A.H., Muench, R.D., 2009. Tides of the northwestern Ross Sea and their impact on dense outflows of Antarctic Bottom Water. *Deep-Sea Research II*, this issue [doi:10.1016/j.dsr2.2008.10.026].
- Price, J.F., O’Neil Baringer, M., 1994. Outflows and deep water production by marginal seas. *Prog. Oceanogr.* 33, 161–200.

- Shapiro, G.I., Hill, A.E., 1997. Dynamics of dense water cascades at the shelf edge. *J. Phys. Oceanogr.* 27, 2381–2394.
- Smagorinsky, J., 1963. General circulation experiments with the primitive equations. I: the basic experiment. *Mon. Weather Rev.* 91, 99–164.
- Smith, P.C., 1975. A streamtube model for bottom boundary currents in the ocean. *Deep-Sea Res.* 22, 853–873.
- Wang, D.-P., 1982. Development of a three-dimensional limited-area (island) shelf circulation model. *J. Phys. Oceanogr.* 12, 605–617.
- Wang, D.-P., 1984. Mutual intrusion of a gravity current and density front formation. *J. Phys. Oceanogr.* 13, 1191–1199.
- Wang, D.-P., 1985. Numerical study of gravity currents in a channel. *J. Phys. Oceanogr.* 15, 299–305.
- Wang, D.-P., Chen, D., Sherwin, T.J., 1990. Coupling between mixing and advection in shallow sea fronts. *Cont. Shelf Res.* 10, 123–136.
- Winton, M., Hallberg, R., Gnanadesikan, A., 1998. Simulation of density-driven fictional downslope flow in Z-coordinate ocean models. *J. Phys. Oceanogr.* 28, 2163–2174.